TOPICAL REVIEW — 2D materials: physics and device applications

# Band gap engineering of atomically thin two-dimensional semiconductors*

Cui-Huan Ge(葛翠环), Hong-Lai Li(李洪来), Xiao-Li Zhu(朱小莉)‡, and An-Lian Pan(潘安练)†

*Key Laboratory for Micro-Nano Physics and Technology of Hunan Province, Key Laboratory for Micro/Nano Optoelectronic Devices of Ministry of Education, State Key Laboratory of Chemo/Biosensing and Chemometrics, School of Physics and Electronics, Hunan University, Changsha* 410082, *China*

(Received 16 December 2016; revised manuscript received 31 January 2017; published online 13 February 2017)

Atomically thin two-dimensional (2D) layered materials have potential applications in nanoelectronics, nanophotonics, and integrated optoelectronics. Band gap engineering of these 2D semiconductors is critical for their broad applications in high-performance integrated devices, such as broad-band photodetectors, multi-color light emitting diodes (LEDs), and high-efficiency photovoltaic devices. In this review, we will summarize the recent progress on the controlled growth of composition modulated atomically thin 2D semiconductor alloys with band gaps tuned in a wide range, as well as their induced applications in broadly tunable optoelectronic components. The band gap engineered 2D semiconductors could open up an exciting opportunity for probing their fundamental physical properties in 2D systems and may find diverse applications in functional electronic/optoelectronic devices.

**Keywords:** 2D semiconductors, band gap engineering, alloys, atomically thin

**PACS:** 42.70.Qs, 71.20.Be, 81.15.Gh, 52.70.Kz **DOI:** 10.1088/1674-1056/26/3/034208

## 1. Introduction

Since the discovery of graphene in 2004, two-dimensional (2D) layered materials have attracted considerable attention in the past decade.[1–5] Atomically thin 2D materials, e.g., $MoS_2$, $WS_2$, $ReS_2$, and $SnS_2$, are burgeoning 2D semiconductor materials for their unique electronic and optical properties.[6–9] Unlike graphene with a zero band gap, these atomically thin 2D materials possess direct band gaps and could give light emission at room temperature, which is important for both electronic and optoelectronic applications. These atomically thin 2D nanosheets derived from the layered materials share many interesting characteristics of the well-known graphene, such as excellent electronic properties, exceptional mechanical flexibility, and partial optical transparency. Furthermore, these 2D nanosheets typically have a well-defined crystalline structure with few surface dangling bonds that traditionally plague most semiconductor nanostructures, and therefore can exhibit excellent electronic properties that are not readily achievable in other semiconductor nanostructures.

Since the application of semiconductor materials is closely related to their band gaps, a vital task in atomically thin 2D semiconductor research is to realize the growth of new 2D materials with tunable band gaps for potential applications in functional electronic/optoelectronic devices.[10–19] Since different atomically thin 2D materials have different band gaps, alloying semiconductors with different band gap variations can be synthesized by controlling the compositional proportions of two or more 2D materials. Thus, the range of band gaps of alloying semiconductors would vary between the minimum and maximum values of the band gaps of all the components. Alloying semiconductors with different band gaps have been widely used in the band gap engineering of bulk semiconductors. For applications in nanoelectronics and nanophotonics, it is very important to achieve semiconductor nanostructures with continuously tuned band gaps.[20–26] Recent advances in 0D and 1D ternary semiconductor structures have shown that their band gaps and light emissions can be tuned gradually by changing their constituent stoichiometries,[27–39] and based on these achieved composition modulated nanostructures, multi-wavelength lasers,[31] wavelength converters,[32] optical diodes,[33] and nanoscale photodetectors[36–38] were realized. For the broad applications in integrated devices and systems, direct growth of these band gap engineered 2D structures should be very important. In this review, we will summarize the recent progress on the band gap engineering of atomically thin two-dimensional semiconductor alloys. Considering from different 2D atomically thin alloys, various research progress will be reviewed systematically.

*Project supported by the National Natural Science Foundation of China (Grant Nos. 11374092, 61474040, 61574054, and 61505051), the Aid Program for Science and Technology Innovative Research Team in Higher Educational Institutions of Hunan Province, China, and the Science and Technology Department of Hunan Province, China (Grant No. 2014FJ2001).

†Corresponding author. E-mail: anlian.pan@hnu.edu.cn

‡Corresponding author. E-mail: zhuxiaoli@hnu.edu.cn

© 2017 Chinese Physical Society and IOP Publishing Ltd 

## 2. $MoS_{2x}Se_{2(1-x)}$ alloys

As two of the most important transition-metal dichalcogenides (TMDs), atomic layered $MoS_2$ and $MoSe_2$ have been extensively studied, due to their atomically thin geometry, unique electronic and optical properties, and potential application integrated nanosystems. For monolayer $MoS_2$ and $MoSe_2$, the direct band gaps are 1.856 and 1.557 eV, respectively. To precisely control the band gap of these 2D TMDs is of central importance for creating optoelectronic devices with tunable spectral responses. Theoretical studies suggested that mixed Mo(S, Se, Te)$_2$ alloys are thermodynamically stable, and thus it is possible to continuously tune their compositions between the constituent limits.[40–43] A cartoon illustrating the atomic structure of a mixed 2D TMDs, along with the constituent parent materials is shown in Fig. 1.[40] In practice, the alloys are modeled by $5\times5$ supercells. Biplab *et al.* have studied in detail the electronic structure of atomically thin uniform 2D $MoS_{2(1-x)}Se_{2x}$ and nanosheets to have an understanding of composition dependent tunability of the electronic and optical properties of these nanosheets.[41] Fatih *et al.* performed DFT calculations to examine the lithium adsorption and diffusion on the hexagonal $MoS_{2(1-x)}Se_{2x}$ monolayers with variation of $x$ for 0.00, 0.33, 0.50, 0.66, and 1.00.[42] In this regard, band gap engineering of 2D alloy $MoS_{2(1-x)}Se_{2x}$ has recently been achieved by using slightly different precursors with different band gaps: (i) mechanically exfoliated $MoS_{2(1-x)}Se_{2x}$ bulk alloy,[44] (ii) creating a composition of mixed alloys by controlling the ratio of the S and Se.[45–62] For example, by using $MoS_2$ and $MoSe_2$ as precursors, Feng *et al.* have successfully synthesized $MoS_{2(1-x)}Se_{2x}$ nanosheets (Fig. 1(b)).[45] A typical scanning electron microscopy (SEM) image of a representative sample shows that the achieved structures are triangular nanosheets with the edge lengths of 30–80 μm (Fig. 1(c)).[46] With Se dopants, some S2 sites become much brighter and display intensities close to or even higher than the Mo sites (Fig. 1(d)), while the intensities of the Mo sites remain unchanged.[47] Figure 1(e) plots x-ray photo-electron spectra of all the synthesized $MoS_{2(1-x)}Se_{2x}$ monolayers.[45] Figure 1(f) shows the normalized Raman spectra of the as-grown $MoS_{2x}Se_{2(1-x)}$ nanosheets with composition x decreasing gradually from 1 (down-most, pure $MoS_2$) to 0 (up-most, pure $MoSe_2$) excited with a 488 nm argon ion laser, respectively.[46] From the curves a to l, the intensity of the S−Mo related modes [$E_{2g(S-Mo)}$, $A_{1g(S-Mo)}$] gradually decreases until they completely disappear, while the Se–Mo related modes [$A_{1g(Se-Mo)}$, $E_{2g(Se-Mo)}$] are absent or very weak at the initial stage and gradually come into appearance with the corresponding intensity increased. Lateral composition graded atomic layered 2D $MoS_{2(1-x)}Se_{2x}$ nanosheets have also been successfully synthesized using a simple moving source thermal evaporation method by an improved CVD route.[51]

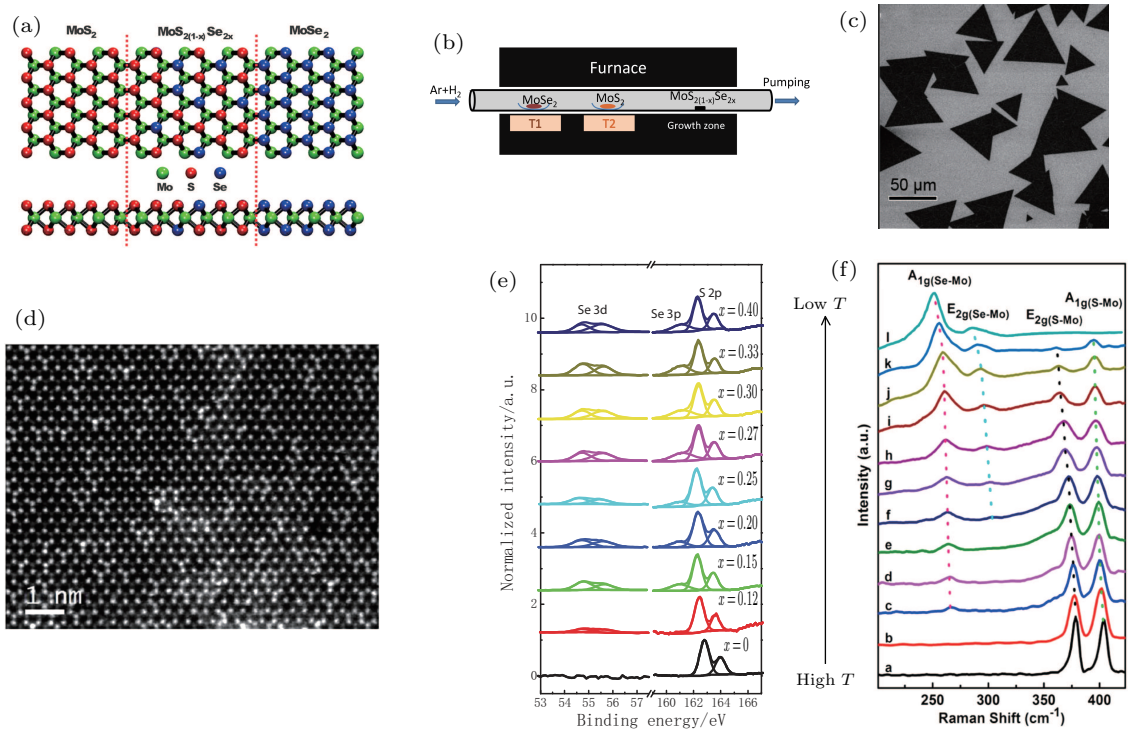



**Fig. 1.** (color online) (a) Top and side views of the atomic structures of MoS2 (left), $MoS_{2x}Se_{2(1-x)}$ alloy (middle), and $MoSe_2$ (right) 2D TMDs. Note that the systems consist of three layers of atoms.[40] (b) Illustration of three-zone furnace for the growth of the $MoS_{2(1-x)}Se_{2x}$ monolayer.[45] (c) Typical SEM morphology of the obtained ternary $MoS_{2x}Se_{2(1-x)}$ nanosheets.[46] (d) ADF image of Se-doped $MoS_2$ with ∼ 12% local Se concentration.[47] (e) XPS of all as-grown $MoS_{2(1-x)}Se_{2x}$ monolayers.[45] (f) Raman spectrum of the $MoS_{2x}Se_{2(1-x)}$ nanosheets excited with a 488 nm argon ion laser.[46]

Figure 2(a) shows the normalized photoluminescence (PL) spectra of the obtained composition modulated $MoS_{2x}Se_{2(1-x)}$ nanosheets excited with a 488 nm argon ion laser.[46] All the samples show single emission bands, with the spectral peaks continuously shifted from 668 nm (for pure $MoS_2$) to 795 nm (for pure $MoSe_2$), which is consistent with the band edge transitions of ternary $MoS_{2x}$ $Se_{2(1-x)}$ thin films. FETs were also fabricated on $MoS_{2(1-x)}Se_{2x}$ monolayers.[45] The $MoS_{2(1-x)}Se_{2x}$ monolayer device exhibited n-type transport behavior with high on/off ratios, and the field-effect mobility $\mu_{FE}$ was also calculated. These electrical measurements confirmed semiconductive behavior for all as-grown $MoS_{2(1-x)}Se_{2x}$ monolayers. As a further characterization of the monolayer alloy, the temperature dependence of the PL was also measured. The $MoS_{0.42}Se_{1.58}$ monolayer of Fig. 2(d) exhibits typical behavior, with the optical gap $E_g$ decreasing with temperature.[56] Figure 2(e) gives the wavelength-selected PL emission mapping of an examined composition graded nanosheet alloy in the spectral regions of 680–690, 710–720, 750–760 nm, respectively.[51] Obviously, the short wavelength region (680–690 nm) is mainly located at the center of the nanosheet, while the long wavelength region (750–760 nm) is mostly located around the edge of sheet.

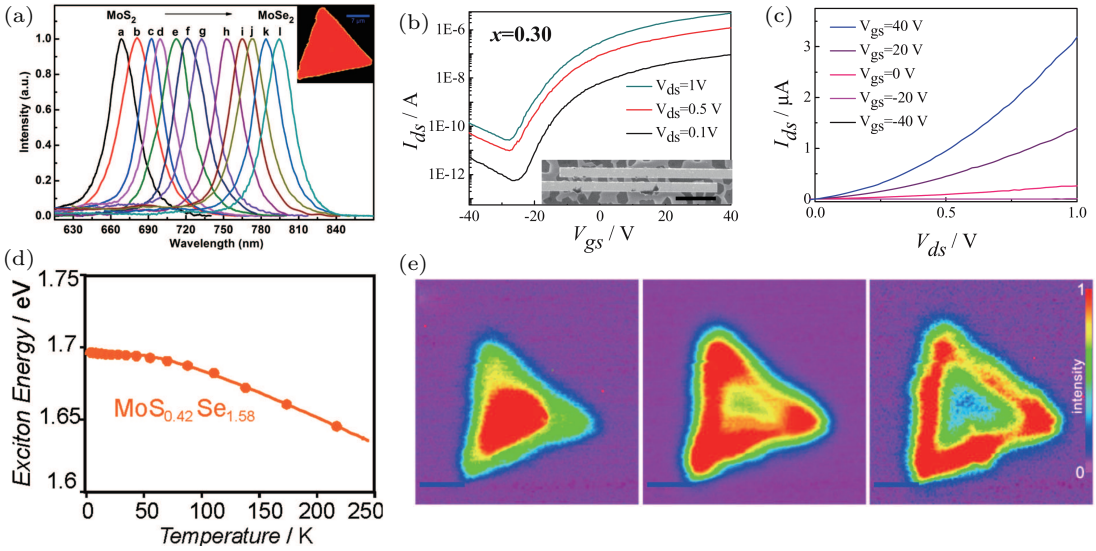



**Fig. 2.** (color online) (a) PL spectrum of the complete composition $MoS_{2x}Se_{2(1-x)}$ nanosheets and a typical PL mapping of a single ternary nanosheet (the inset, scale bar, 7 μm) excited with a 488 argon ion laser.[46] (b), (c) Source–drain current to the gate voltage ($I_{ds}$–$V_{gs}$) and the source–drain current to the source–drain voltage ($I_{ds}$–$V_{ds}$) for FETs containing the $MoS_{2(1-x)}Se_{2x}$ monolayer for $x = 0.30$.[45] The inset shows the SEM image of the device channel. Scale bar is 5 μm. (d) The exciton emission energy as a function of the temperature of the monolayer alloy.[56] (e) Wavelength-dependent PL mapping of a single composition graded nanosheet alloy in the spectral regions of 680–690, 710–720, 750–760 nm, respectively (scale bars, 5 μm).[51]

## 3. $WS_{2(1-x)}Se_{2x}$ alloys

Except for $MoS_{2x}Se_{2(1-x)}$, atomically thin 2D $WS_{2x}Se_{2(1-x)}$ alloy has also attracted wide range of interest. The schematic illustration in Fig. 3(a) shows the transformation from $WO_3$ (monoclinic crystal) to $WS_{2(1-x)}Se_{2x}$ (hexagonal crystal) through simultaneous sulfurization and selenization.[62] Figure 3(b) illustrates a single-zone furnace utilized in the growth of the monolayer $WSe_{2(1-x)}S_{2x}$. Because of the much higher chemical activity of S atoms than Se atoms, it is possible to tune the contents in the monolayer $WSe_{2(1-x)}S_{2x}$ by only varying the precursor weight of sulfur powder. The resulting alloy nanosheets are typically monolayers with a well-defined triangular shape, as identified by optical contrast and atomic force microscopy studies (Fig. 3(c)).[64] HRSTEM was utilized to characterize the monolayer $WS_{2(1-x)}Se_{2x}$, which shows the $Z$-contrast ($Z$ is the atomic number) as images with atomic-scale resolution, as observed in Fig. 3(d).[62] The hexagonal rings of the alternative W and S/Se atoms in each unit. There are three levels of brightness in Fig. 3(d). The dimmest spots represent the S + S atoms, which are encircled in red; the relatively bright spots are the S + Se atoms, which are encircled in yellow; and the even brighter spots are the Se+Se atoms, which are encircled in blue. Figure 3(e) shows the spatially resolved EDS elemental mapping of the S, Se, and W elements of a typical $WS_{2(1-x)}Se_{2x}$ alloy, all elements show relatively uniform distribution across a triangular domain, indicating composition uniformity throughout the entire domain.[64] To further investigate the structural evolution in the $WS_{2x}Se_{2-2x}$ alloy nanosheets, the Raman spectra from the same sample series were collected.[64] The Raman spectra display five main modes for most $WS_{2x}Se_{2-2x}$ nanosheets, which can be assigned to $A_{1g(SW)}$ mode (401.9–419.7 $cm^{-1}$), $A_{1g(SeW)}$ mode (251.6–264.7 $cm^{-1}$), $A_{1g(S-W-Se)}$ mode (379.5–385.2 $cm^{-1}$), $E_{2g(SW)}$ mode (∼ 354.7–355.9 $cm^{-1}$), and $E_{2g(SW)}$–$LA_{(SW)}$ + $A_{1g(SeW)}$–$LA_{(SeW)}$ mode (135.2–172.5 $cm^{-1}$).

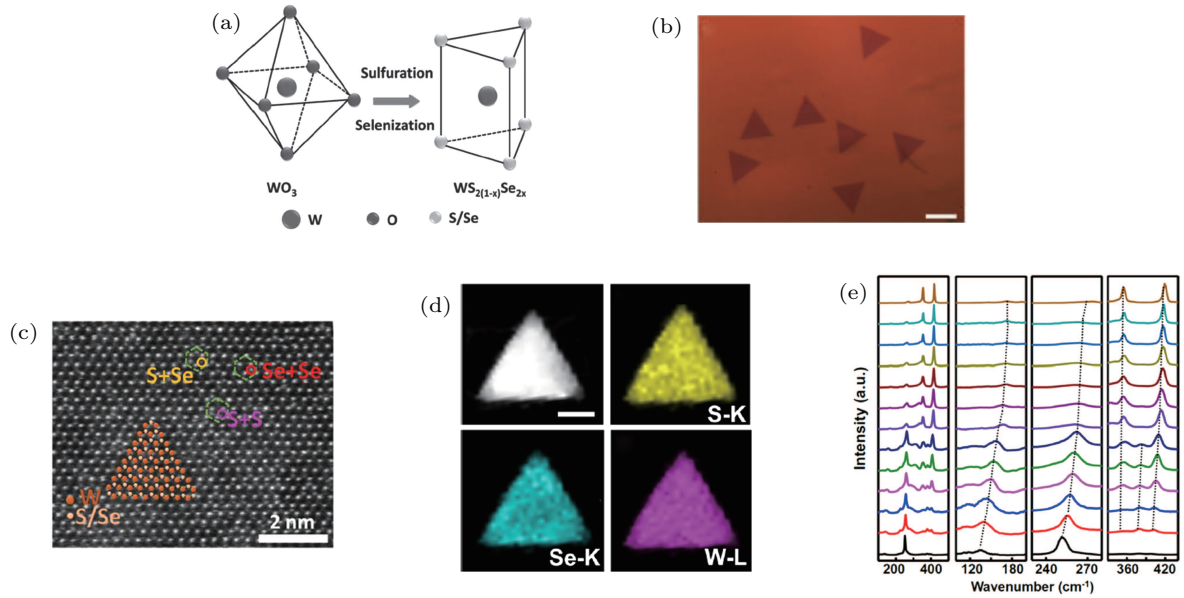



**Fig. 3.** (color online) (a) Schematic illustration of the transformation from $WO_3$ (monoclinic crystal) to $WS_{2(1-x)}Se_{2x}$ (hexagonal crystal) through simultaneous sulfurization and selenization processes.[62] (b) Optical microscopy image of typical $WS_{2x}Se_{2-2x}$ nanosheets ($x = 0.454$; scale bar = 20 μm.[64] (c) HRSTEM image of the as-grown monolayer $WS_{2(1-x)}Se_{2x}$ ($x = 0.43$).[42] (d) HAADF image of a small $WS_{2x}Se_{2-2x}$ domain ($x = 0.573$; scale bar = 500 nm) and EDS mapping of the same triangular domain for S–K line, Se–K line, and W–L line, respectively.[64] (e) Evolution of Raman spectra in the $WS_{2x}Se_{2-2x}$ monolayer nanosheets as a function of chemical composition: full-range Raman spectra, $E_{2g(S-W)}$–$LA_{(SW)}$ + $A_{1g(SeW)}$–$LA_{(SeW)}$ mode, $A_{1g}$ of Se–W mode, and $E_{2g}$ of S–W mode, $A_{1g}$ of S–W–Se mode, and $A_{1g}$ of S–W mode.[64]

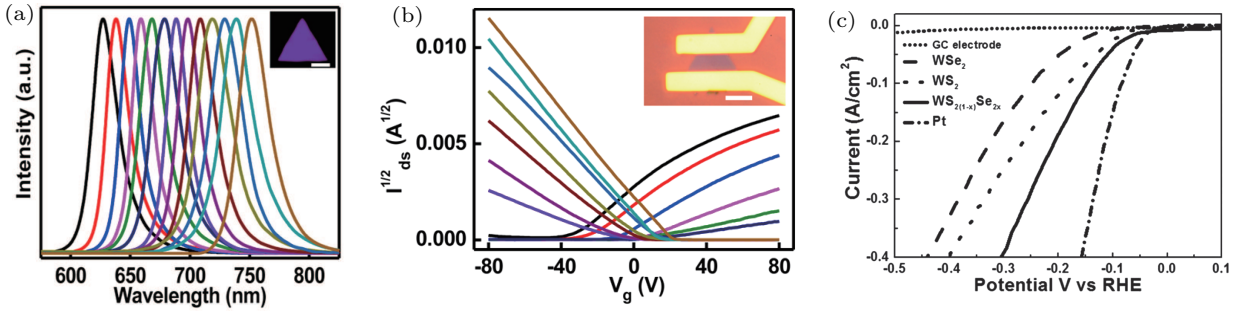



**Fig. 4.** (color online) (a) Photoluminescence spectra of a series of composition tunable $WS_{2x}Se_{2-2x}$ monolayer nanosheets. Inset: photoluminescence intensity mapping of the same $WS_{2x}Se_{2-2x}$ nanosheets ($x = 0.522$; mapping peak is 687.5 nm; scale bar is 10 μm).[64] (b) Transfer characteristics ($I_d^{1/2}$–$V_g$ plot) of $WS_{2x}Se_{2-2x}$ nanosheet transistors with different S atomic ratios from nearly pure $WSe_2$ (brown curve) to nearly pure $WS_2$ (black curve).[64] (c) Polarization curves after iR correction obtained at a voltage sweeping rate of 5 mV·s$^{-1}$ in the monolayer $WS_{2(1-x)}Se_{2x}$ ($x = 0.43$), monolayer $WS_2$, monolayer $WSe_2$, Pt and GC electrode.[62]

To investigate the band gap modulation in the resulting alloy nanosheets, $\mu$-PL spectra were taken using a micro-Raman microscope and spectrometer excited by a 488 nm argon ion laser (power is 5 μW) in ambient condition. Photoluminescence studies demonstrate that all the monolayer samples display prominent emission with a single sharp peak with full width at half maximum (fwhm) about 25 nm. The PL spectral peak positions are continuously tunable from 626.6 nm (nearly pure $WS_2$) to 751.9 nm (nearly pure $WSe_2$) depending on the exact synthetic conditions (Fig. 4(a)).[64] Furthermore, the spatially resolved mapping of the PL intensity also shows a highly uniform contrast (inset), demonstrating highly uniform optical properties and crystalline quality. To probe the electronic properties of the as-grown monolayer $WSe_{2(1-x)}S_{2x}$ alloy, gated-FET devices based on the monolayer $WSe_{2(1-x)}S_{2x}$ alloy by the EBL was fabricated by Yang *et al*.[63] The typical current-voltage ($I_{ds}$–$V_{ds}$) plots of the FET devices indicates the increase of the drain current by decreasing the back-gate voltage. The band gap tuning capability is ∼ 120 meV by varying the S content in the monolayer $WSe_{2(1-x)}S_{2x}$ alloy. The top-gated FET configuration improves the carrier mobility with two orders larger than that in the back-gated FET device. The evolution of electrical properties and FET threshold voltages can be more clearly seen from an $I_{sd}^{1/2}$–$V_g$ plot under a source-drain bias of 3 V for the nanosheets with increasing sulfur atomic ratio from nearly pure $WSe_2$ (brown curve) to nearly pure $WS_2$ (black curve, Fig. 4(b)).[64] For the $WSe_2$-rich alloys (∼ 0–0.55 S atomic ratio), the FETs predominantly display p-type semiconductor properties, whereas for the $WS_2$-rich alloys (∼ 0.55–1 S atomic ratio), the n-type semiconductor properties are mainly observed. The polarization curves (Fig. 4(c)) after internal resistance (iR) compensation obtained at a scan rate of 5 mV·s$^{-1}$ show the normalized current density as a function of the voltage versus RHE in

the monolayer $WS_{2(1-x)}Se_{2x}$ ($x = 0.43$), $WS_2$, $WSe_2$, Pt, and bare GC electrode. Impressively, the monolayer $WS_{2(1-x)}Se_{2x}$ electrode exhibits the significant HER catalytic activity with the lowest onset overpotential of $\approx 80$ mV compared to $WS_2$ (100 mV) and $WSe_2$ (150 mV).

## 4. $WMoS_2$ alloys

2D $MoS_2$ and $WS_2$ can alloy to form atomically thin 2D $WMoS_2$ alloy.[65–75] Similar to $MoS_2$ and $WS_2$, $Mo_{1-x}W_xS_2$ alloy has a layered structure, and each layer consists of two hexagonal S atom layers and a sandwiched Mo/W atom layer. The Mo or W atom sits in the center of a trigonal prismatic cage formed by six S atoms (Fig. 5(a)).[65] The two metal species form homo-nuclear chains along the edges of the triangular $W_xMo_{1-x}S_2$ alloys. Hydrostatic pressure up to 40 GPa was applied to $Mo_{0.5}W_{0.5}S_2$ layered ternary compound to study the vibrational modes and understand the phonon and lattice distortion for high compressive forces.[71] With increasing pressure, the in-plane $E_{2g}$ modes and out-of-plane $A_{1g}$ modes follow closely to that of pristine $MoS_2$ or $WS_2$. The band gap of $Mo_{1-x}W_xS_2$ monolayers could be tuned by $MoS_2$ or $WS_2$ composition, which was evidenced by PL measurements.[65] As W composition $x$ increases, the A exciton emission ($\sim$ 1.8–2.0 eV) red shifts and then blue shifts (Fig. 5(b)). For $Mo_{1-x}W_xS_2$ monolayer alloys, the PL spectra show one strong PL peak, i.e. A-exciton emission (low-energy one), with a weak shoulder B-exciton emission peak at the higher energy side.[67] The PL intensities of the $Mo_{1-x}W_xS_2$ monolayer alloys first decrease (due to electron–phonon interaction) and then increase with temperature increasing. Figure 5(c) presents a schematic diagram of the $Mo_{0.5}W_{0.5}S_2$ photoresistor that was constructed from a PLD-grown film using the wire-masking technique.[68] There are no sampling points at the rise and decay edges from the temporal switching cycle, indicating that the response time of the device is shorter than 150 ms, which is the sampling limit of the measurement system. While alloy scattering was found to be important for alloy compositions $0.5 < x < 0.7$, the mobility is found to be limited by LO phonon scattering across the entire range of compositions except for the combination of Mo-rich alloys with very low 2D carrier densities ($10^{12}$ cm$^{-2}$), where the impurity scattering dominates.[69] The morphology, elemental composition, bonding information, and electrocatalytic properties toward hydrogen evolution reaction (HER) of 3D electrodes coated with $Mo_xW_{1-x}S_2$ alloys with different Mo/W ratios were also studied.[73]

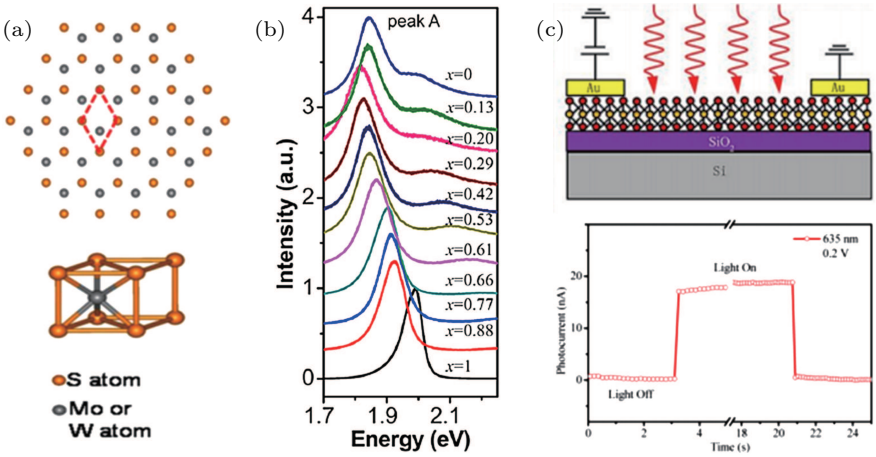



**Fig. 5.** (color online) (a) Top view of $Mo_{1-x}W_xS_2$ monolayer and a side view of a unit cell.[65] (b) PL spectra of $Mo_{1-x}W_xS_2$ monolayers with different W compositions $x$.[65] (c) Schematic diagram of a $Mo_{0.5}W_{0.5}S_2$ photoresistor and a temporal switching cycle of the $Mo_{0.5}W_{0.5}S_2$ photodetector under a 635 nm illumination.[68]

## 5. $Mo_{1-x}W_xSe_2$ alloys

Triangular $Mo_{1-x}W_xSe_2$ monolayers[76–79] with tens of microns in size were successfully grown on $SiO_2$/Si substrates at 780 °C by a low pressure CVD method. According to the simulation, the dimmed Se sites correspond to Se vacancies (VSe) where one Se atom at the site is missing (Fig. 6(a)).[76] Figure 6(b) shows the atomic force micro-scopy (AFM) image of $Mo_{0.67}W_{0.33}Se_2$ sheets, meaning the height of the monolayer alloy is about 1.3 nm.[78] Figure 6(c) shows an HAADF STEM image of $Mo_{0.47}W_{0.53}Se_2$ flakes. An atomically resolved image revealed its honeycomb atom arrangement, as shown in the inset of Fig. 6(c).[78] PL measurements on $Mo_{1-x}W_xSe_2$ monolayers with different W compositions showed tunable band gap exciton emissions (Fig. 6(d)).[78] As W composition $x$ increases, the PL emission shows a bowing effect, in which emission energy first red shifts to a minimum value at around $x = 0.2$–$0.3$ and then monotonically blue shifts. Therefore, the band gap emission of the $Mo_{1-x}W_xSe_2$ monolayers can be continuously tuned from 1.56 eV (reached $x = 0.21$) to 1.65 eV (reached $x = 1$). Figure 6(e) shows unpo-

larized Raman spectra of $Mo_{1-x}W_xSe_2$ monolayers with different W composition $x$ and the corresponding composition-dependent Raman frequencies.[78] The $MoSe_2$-like $E_{2g}$ shifts to lower frequency as the W composition increases. In addition, the second order Raman peaks also shift and showed two-mode behaviors as the W composition changes. Figure 6(f) shows the dynamics of excitons in $MoSe_2$, $Mo_{0.98}W_{0.02}Se_2$, and $Mo_{0.82}W_{0.18}Se_2$ acquired by exciting the monolayers with a $\approx 300$ fs pump pulse having a central wavelength of 620 nm and an energy fluence of $\approx 0.9$ μJ·cm$^{-2}$.[76] The room temperature PL intensity from $Mo_{0.82}W_{0.18}Se_2$ monolayers is $\approx 10$ times stronger than that from $MoSe_2$, accompanied by a longer exciton lifetime, indicating the decrease of defect-mediated nonradiative recombination. The calculated mobility of $Mo_{1-x}W_xSe_2$ monolayer FETs with $x = 0.39$ was about $7.8 \times 10^{-2}$ cm$^2$·V$^{-1}$·s$^{-1}$.[78]

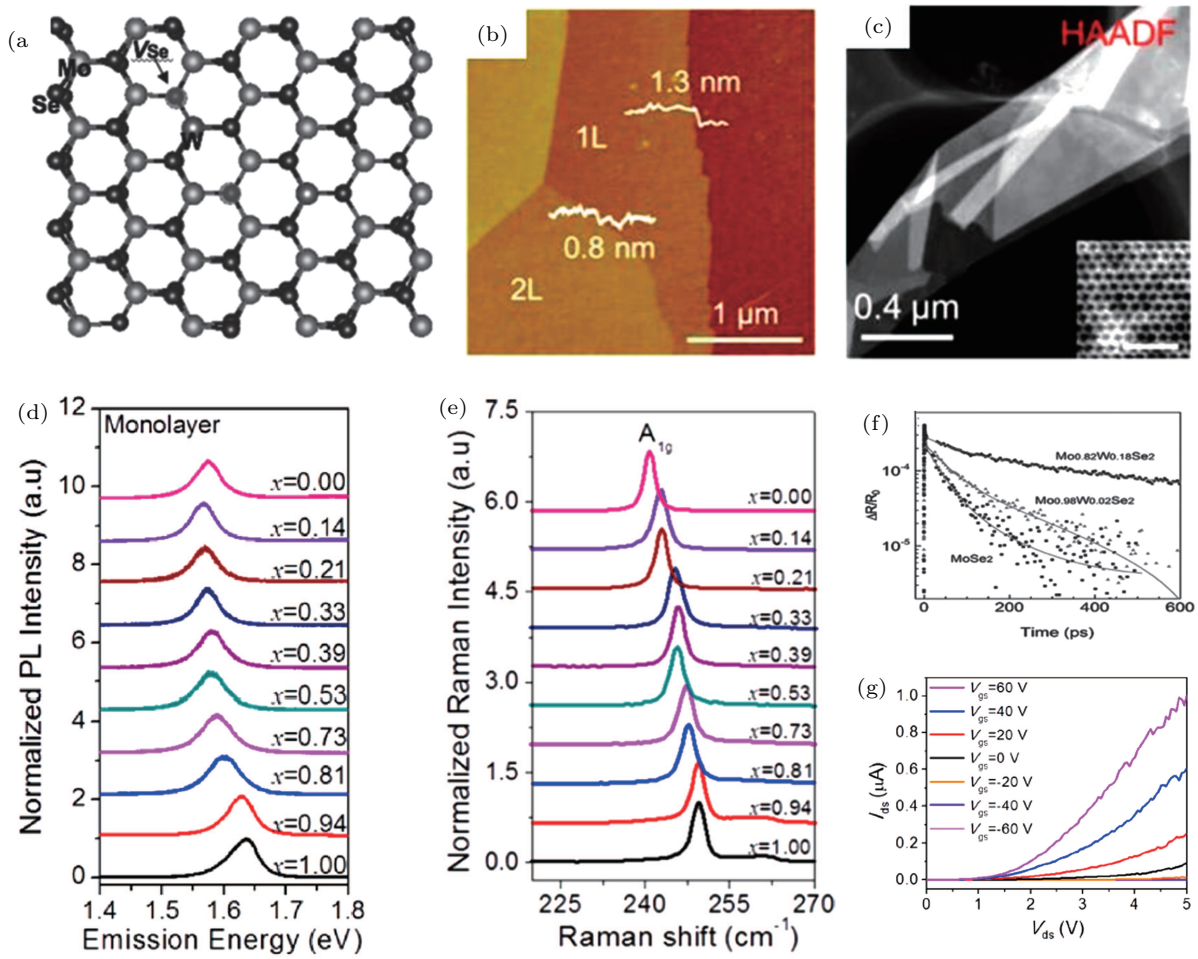



**Fig. 6.** (color online) (a) Top view of the atomic model corresponding to the $Mo_{0.82}W_{0.18}Se_2$ monolayer.[76] (b) AFM image of $Mo_{0.67}W_{0.33}Se_2$ sheets.[78] (c) HAADF STEM image of $Mo_{0.47}W_{0.53}Se_2$ flakes. Inset in panel (c) is a high-resolution STEM image, and the scale bar is 3 nm.[78] (d) Composition-dependent PL spectra of $Mo_{1-x}W_xSe_2$ monolayer alloys.[78] (e) Raman spectra of $Mo_{1-x}W_xSe_2$ monolayers with different W composition $x$.[78] (f) Differential reflection signal (scattered dots) measured from $MoSe_2$, $Mo_{0.98}W_{0.02}Se_2$, and $Mo_{0.82}W_{0.18}Se_2$ monolayers with a 620 nm pump and a 800 nm probe pulse.[76] Solid curves are biexponential decay fits.[76] (g) Output curves ($I_{ds}$–$V_{ds}$) under different bottom gate voltages of $Mo_{1-x}W_xSe_2$ monolayer FETs for $x = 0.39$.[78]

## 6. TMDs alloys with Te

Unlike other TMDs, $MoTe_2$ and $WTe_2$ are distinguished by the existence of a semimetallic distorted octahedral T′ phase with a very small energy barrier from the semiconducting H phase.

The calculations by Rajbanshi *et al.* showed that $MoS_{2(1-0.5)}Te_{2(0.5)}$ has a direct band gap structure, both the highest occupied molecular orbital (HOMO) and lowest unoccupied molecular orbital (LUMO) are approaching toward the Fermi level with the increase of doping percentage.[41] The formation energy diagram in Fig. 7(a) shows that the T′ phase of pristine monolayer $WTe_2$ is thermodynamically more favorable, while monolayer $MoTe_2$ is more stable in the H structure due to different contributions from ligand field splitting stabilization and CDW stabilization.[80] It is found that in monolayer $W_xMo_{1-x}Te_2$ alloy, the energy difference between the T′ phase and the H phase is reduced when $x$ approaches the transition point indicating the potential that a smaller amount of charge modulation than that in pristine $MoTe_2$ can render the T′ phase more stable than the H phase of monolayer $W_xMo_{1-x}Te_2$ when $x$ is closer to 0.333. At some chosen temperature $T$, the two phases' Gibbs or Helmholtz free energies form a free

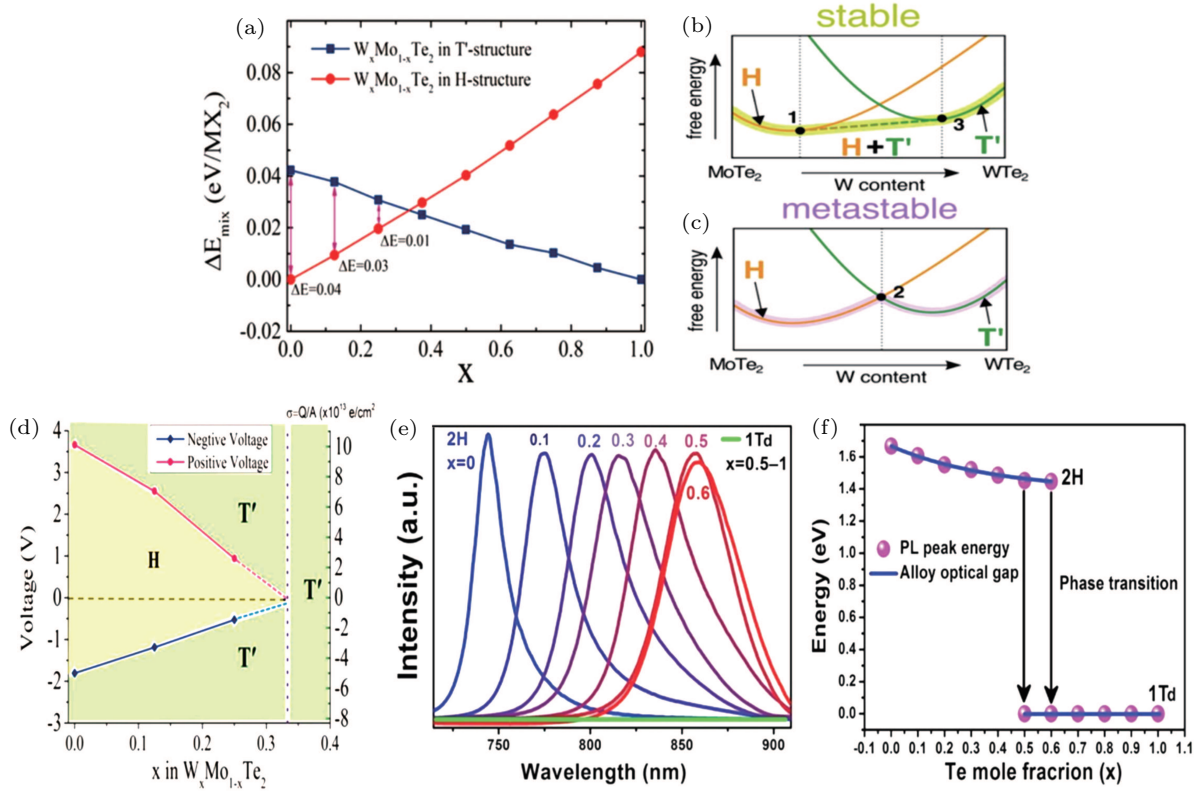



**Fig. 7.** (color online) (a) Formation energy of $W_xMo_{1-x}Te_2$ in both T′ structure (blue) and H structure (red) at various W concentration $x$.[80] (b), (c) Free energy landscape at fixed temperature.[81] (d) Positive (pink) and negative (blue) voltage required to switch the relative stability of H-$MoTe_2$ and T′-$MoTe_2$.[80] (e), (f) The photoluminescence (PL) spectra of monolayer $WSe_{2(1-x)}Te_{2x}$ ($x$ = 0–1.0) alloys.[82]

energy landscape that allows determination of which phase or phase mixture minimizes total free energy as a function of W content. Panel (Fig. 7(b)) follows the thermodynamically stable convex hull: the monolayer minimizes its total free energy by existing in the H phase on the left-hand side of point 1, as single phase T′ on the right-hand side of point 3, and as a two-phase coexistence of a W-depleted H phase and a W-rich T′ phase between points 1 and 3. Panel (Fig. 7(c)) applies when long-ranged W diffusion across phases is quenched. Point 2 then marks the transition between metastable single-phase H and metastable single-phase T′.[61] The converted critical voltages required to trigger the phase transition between the H and the T' phase of monolayer $W_xMo_{1-x}Te_2$ alloy with different compositions are shown in Fig. 7(d).[80] A fast switching device structure is proposed and reasonable critical gate voltages required to induce the phase transition are estimated by a simple capacitor model. The PL spectra of 2H $WSe_{2(1-x)}Te_{2x}$ ($x$ = 0–0.6) monolayer samples excited with a 532 nm laser are collected and shown in Fig. 7(e).[82] All monolayer 2H $WSe_{2(1-x)}Te_{2x}$ show the emission bands, and the spectral peak continuously shifts from 744 nm (pure $WSe_2$) to 857 nm (near infrared). For 1Td sample, as expected, no PL signal is detected when $x \geq 0.6$. Figure 7(f) plots the optical gap versus mole fraction of Te for monolayer $WSe_{2(1-x)}Te_{2x}$.[82] The band gaps are continuously shifted from 1.67 eV (pure $WSe_2$) to 1.44 eV.

## 7. 2D alloys with Ga

The band gap for GaS, GaSe and and GaTe monolayers as 2.5, 2.1, and 1.7 eV (on average), respectively. In Fig. 8(a), wafer-scale $GaTe_xSe_{1-x}$ films are successfully grown by MBE.[83] Ga, Te, and Se elements distribute uniformly over a large range of 0.16 mm×0.16 mm. $GaS_{1-x}Se_x$ multilayers with tunable compositions over the entire range have been successfully synthesized by CVT (Fig. 8(b)).[84] Figure 8(c) displays the UV–visible diffuse reflectance spectrum measured for various compositions of $GaS_{1-x}Se_x$ multilayered nanosheets.[84] The onset of the absorption band, the indirect band gap obtained from the K–M plots, and the PL peak position (at 8 K) all show a linear dependence on the composition, with similar band gap ($E_g$) values for any given value of $x$ (Fig. 8(d)).[84] Figure 8(e) shows a schematic view of the fabricated $GaSe_{0.5}Te_{0.5}$ nanoflake device.[85] The $GaSe_{0.5}Te_{0.5}$ nanoflake photodetectors show extended light response wavelength compared to GaSe (Fig. 8(f)). Also, with increasing Te composition the photocurrent of $GaTe_xSe_{1-x}$ alloys has a rising trend.[83]

## 8. 2D alloys with Re

Re dichalcogenides are promising candidates for the study of anisotropy. $ReS_2$ forms a distorted 1T structure with triclinic symmetry (Fig. 9(a)).[86] Figure 9(b) shows the absorption spectra of $ReS_2$, ReSSe and $ReSe_2$, respectively.

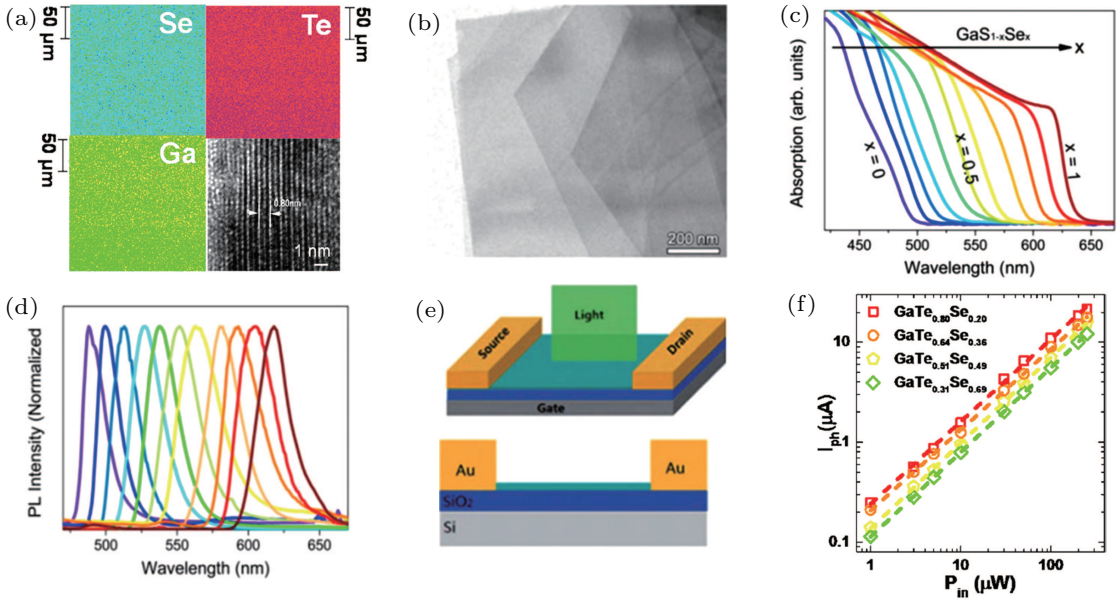



**Fig. 8.** (color online) (a) EDX mapping of Se, Te, and Ga in a $GaTe_{0.25}Se_{0.75}$ film.[83] (b) TEM images of GaS multilayered nanosheets.[84] (c), (d) UV visible diffuse reflectance spectrum (in absorption) and PL spectrum (at 8 K) of the $GaS_{1-x}Se_x$ nanosheets with various values of $x$.[84] (e) Three-dimensional schematic view and the cross section view of the $GaSe_{0.5}Te_{0.5}$ nanoflake device.[85] (f) Composition-dependent photocurrent of $GaTe_xSe_{1-x}$ alloys under different laser intensities.[83]

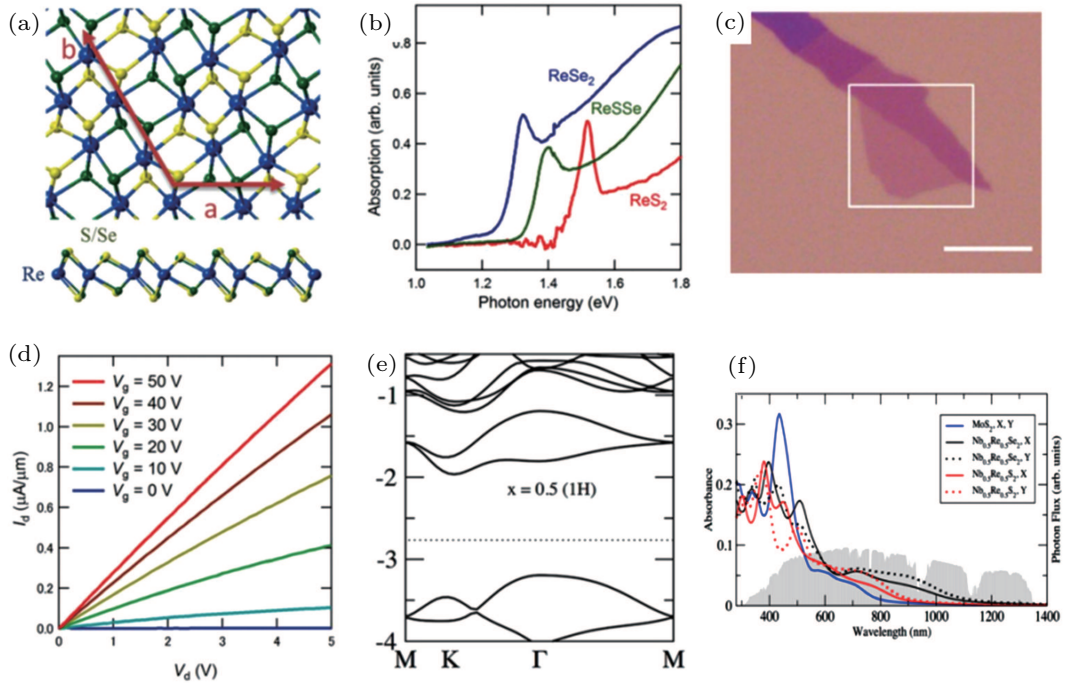



**Fig. 9.** (color online) (a) Crystal structure of the $ReX_2$ compound.[86] (b) Absorption spectrum of $ReS_2$, ReSSe, and $ReSe_2$.[86] (c) Typical optical image of a ReSSe flake with regions of different thicknesses. Scale bar: 10 μm.[86] (d) $I_d$–$V_d$ curve of a ReSSe thin-flake transistor with a thickness of about 3 nm.[86] (e) Band structures of $Nb_xRe_{1-x}S_2$ systems ($x = 0.5$).[87] (f) Derived absorbance along in-plane directions.[87]

Figure 9(c) shows a typical optical image of ReSSe flakes, with thicknesses ranging from monolayer to four layers. A field-effect transistor based on a ReSSe thin flake with a thickness of about 3 nm was fabricated and studied (Fig. 9(d)). The $I_d$–$V_d$ data exhibit a slight super linear behaviour at low drain bias, which suggests that the electrons are injected through a Schottky barrier at the metal–semiconductor interface. Photosensitive devices based on few-layer ReSSe exhibit a very high photoresponsivity, up to 8 $A{\cdot}W^{-1}$.

With $x_{Re} = 0.5$, the concentrations of groups 5 and 7 transition metals are equal and thus $Nb_{0.5}Re_{0.5}S_2$ is valence isoelectronic to $MoS_2$. Mirroring $MoS_2$, $Nb_{0.5}Re_{0.5}S_2$ is a semiconductor albeit with a smaller band gap and has competing CB minima and VB maxima at the $\Gamma$ and $K$ points (Fig. 9(e)).[87] Figure 9(f) shows the absorbance of the TMDs overlaid onto the solar spectrum.[87] From first principle cal-

culations, these alloy TMDs possess significantly smaller band gaps, which are close to the optimal value of 1.3 eV for efficient solar absorption and show enhanced solar absorption in the visible range of the solar spectrum.

## 9. Other 2D alloys

Dopping is another effective method to tune the band gap of semiconductor materials. A number of experimental and theoretical studies have been committed to the atomically thin 2D alloys by dopping in recent years.[88–96] Figure 10(a) is the hexagonal bilayer $Co_{0.16}Mo_{0.84}S_2$ nanosheet synthesized by the CVD method.[88] The $A_{1g}$ mode and $E_{2g}$ modes show one-mode and two-mode behaviors, respectively. The $Co_xMo_{1-x}S_2$ nanosheet devices demonstrated FET characteristics of a n-type semiconductor (Fig. 10(b)), with a mobility as high as 0.52 $cm^2/(V{\cdot}s)$, the on/off ratio (about 10) is lower than the reported bilayer $MoS_2$ flakes.[88] Meanwhile, good quality $Sn_{1-x}Mn_xSe_2$ films with relatively high Mn concentrations have been successfully grown by MBE on GaAs (111)B substrates.[89] The XRD patterns for the $Sn_{1-x}Mn_xSe_2$ films are shown in Fig. 10(c). The samples show only (00l) peaks of the $SnSe_2$ structure, illustrating excellent c-axis-oriented epitaxial growth. Figure 10(d) shows the Mn concentration as a function of Mn effusion cell temperature $T_{Mn}$. One can see that the Mn concentration increases linearly from about 42% to 66% as $T_{Mn}$ increases from 670 °C to 760 °C. The electronic and magnetic properties of Mn-doped monolayer $WS_2$ were also investigated by Zhao et al.[90] According to their simulation calculations, a significant portion of the alloy's spin density is localized on the Mn atom. For each considered Mn-doped $WS_2$ configuration, the formation energy is lower under S-rich conditions, which indicates that it is energy favorable and relatively easier to incorporate Mn atom into $WS_2$ nanosheet under S-rich experimental conditions. In addition, Deniz *et al*. investigated the electronic and magnetic properties of a $ReS_2$ monolayer substitutionally doped with transition metal and nonmetal atoms.[91] The mixed-metal fere crystal compounds, $[(SnSe)_{1.16-1.09}]_1[(Nb_xMo_{1-x})Se_2]_1$ with $x = 0$, 0.26, 0.49, 0.83, and 1, were successfully produced via adaptation of the modulated elemental reactant method.[93] Template-based sputtering method is used first to fabricate Au nanoantenna (NA)/MoS2 heterostructures with an enhanced exciton energy.[95] The PL spectrum red-shifting and intensity attenuation happen in the n-type doping of GQD/$MoS_2$ heterostructure configuration based on optical doping mechanism.[96]

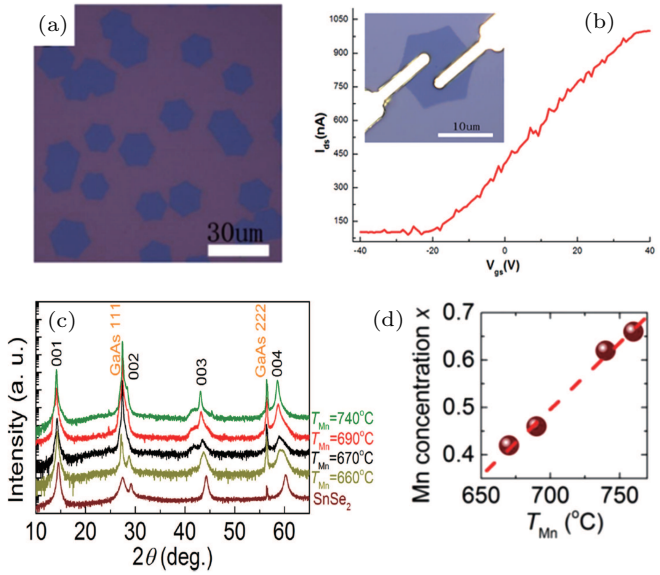



**Fig. 10.** (color online) (a) Optical image of the $Co_{0.16}Mo_{0.84}S_2$ nanosheets on the substrate.[88] (b) Room-temperature characteristics of the $Co_xMo_{1-x}S_2$ nanosheet FET devices with 2 V applied bias voltage. The inset shows the optical image of a FET device.[88] (c) XRD spectra of $Sn_{1-x}Mn_xSe_2$ films grown with different values of $T_{Mn}$.[89] (d) Mn effusion cell temperature dependences of the Mn concentration.[89]

In conclusion, great progress has been made in recent years in search for the band gap engineering of atomically thin 2D semiconductor alloys. Up to now, almost all kinds of 2D semiconductor alloys have been obtained, and recent studies have shown exciting potential of these atomically thin semiconductor alloys, including the demonstration of atomically thin transistors, a new design of vertical transistors, as well as new types of optoelectronic devices such as tunable photovoltaic devices and light emitting devices. In addition to the growth and corresponding device applications, it is equally important to pursue the novel physical properties of the band gap engineered 2D nanosheets and use them in new 2D semiconductor-based functional device designs.

Although the progress achieved in band gap engineering of atomically thin 2D semiconductor nanosheets represents only an initial success in this new field of material science research. Many new opportunities and challenges remain in the coming years, such as the instability of 2D semiconductor alloys in the air, which is still the key problem when things come to related material applications. Is there any way to make the raw materials more harmless in order to fit with the requirements of the environment? We are looking for the answers.

Above all, through the tireless efforts of researchers and the development of research technology, alloys from other 2D materials, such as 2D metal halide, and 2D black phosphorus which attracts great attention lately will gradually enter the people's vision in the near future.

## References

[1] Zhang L, Yu J, Yang M, Xie Q, Peng H and Liu Z 2013 *Nat. Commun.* **4** 1443

[2] Freitag M, Low T, Zhu W, Yan H, Xia F and Avouris P 2013 *Nat. Commun.* **4** 1951

[3] Weiss N O, Zhou H, Liao L, Liu Y, Jiang S, Huang Y and Duan X 2012 *Adv. Mater.* **24** 5782

[4] Yan K, Wu D, Peng H, Jin L, Fu Q, Bao X and Liu Z 2012 *Nat. Commun.* **3** 1280

[5] Yan H, Li X, Chandra B, Tulevski G, Wu Y, Freitag M, Zhu W, Avouris P and Xia F 2012 *Nat. Nanotechnol.* **7** 330

[6] Radisavljevic B, Radenovic A, Brivio J, Giacometti V and Kis A 2011 *Nat. Nanotech.* **6** 147

[7] Voiry D, Yamaguchi H, Li J, Silva R, Alves D, Fujita T, Chen M, Asefa T, Shenoy V, Eda G and Chhowalla M 2013 *Nat. Mater.* **12** 850

[8] Tongay S, Sahin H, Ko C, Luce A, Fan W, Liu K, Zhou J, Huang Y, Ho C, Yan J, Ogletree D F, Aloni S, Ji J, Li S, Li J, Peeters F M and Wu J 2014 *Nat. Commun.* **5** 3252

[9] Liu J, Xia C, Li H and Pan A 2016 *Nanotechnology* **27** 34LT01

[10] Gong Y, Lin J, Wang X, Shi G, Lei S, Lin Z, Zou X, Ye G, Vajtai R, Yakobson B, Terrones H, Terrones M, Tay B K, Lou J, Pantelides S T, Liu Z, Zhou W and Ajayan P M 2014 *Nat. Mater.* **13** 1135

[11] Duan X, Wang C, Shaw J, Cheng R, Chen Y, Li H, Wu X, Tang Y, Zhang Q, Pan A, Jiang J, Yu R, Huang Y and Duan X F 2014 *Nat. Nanotechnol.* **9** 1024

[12] Li M, Shi Y, Cheng C, Lu L, Lin Y, Tang H, Tsai M, Chu C, Wei K, He J, Chang W, Suenaga K and Li L 2015 *Science* **349** 524

[13] Huang C, Wu S, Sanchez A, Peters J, Beanland R, Ross J, Rivera P, Yao W, Cobden D and Xu X 2014 *Nat. Mater.* **13** 1096

[14] Zhang X, Lin C, Tseng Y, Huang K and Lee Y 2014 *Nano Lett.* **15** 410

[15] Gong Y, Lei S, Ye G, Li B, He Y, Keyshar K, Zhang X, Wang Q, Lou J, Liu Z, Vajtai R, Zhou W and Ajayan P M 2015 *Nano Lett.* **15** 6135

[16] Duan X, Wang C, Pan A, Yu R and Duan X 2015 *Chem. Soc. Rev.* **44** 8859

[17] Xie L M 2015 *Nanoscale* **7** 18392

[18] Shi Y, Li H and Li L J 2015 *Chem. Soc. Rev.* **44** 2744

[19] Kutana A, Penev E S and Yakobson B I 2014 *Nanoscale* **6** 5820

[20] Pan A, Yang H, Liu R, Yu R, Zou B and Wang Z 2005 *J. Am. Chem. Soc.* **127** 15692

[21] Pan A, Yang H, Yu R and Zou B 2006 *Nanotechnology* **17** 1083

[22] Pan A, Liu R, Wang F, Zou B, Zacharias M and Wang Z 2006 *J. Phys. Chem. B* **110** 22313

[23] Pan A, Wang X, He P, Zhang Q, Wan Q, Zacharias M, Zhu X and Zou B 2007 *Nano Lett.* **7** 2970

[24] Pan A L, Yao L, Qin Y, Yang Y, Kim D S, Yu R, Zou B, Werner P, Zacharias Z and Goesele U 2008 *Nano Lett.* **8** 3413

[25] Pan A, Liu R, Sun M and Ning C 2009 *J. Am. Chem. Soc.* **131** 9502

[26] Pan A, Liu R, Sun M, Sun M and Ning C 2010 *ACS Nano* **4** 671

[27] Gu F, Yang Z, Yu H, Xu J, Wang P, Tong L and Pan A 2011 *J. Am. Chem. Soc.* **133** 2037

[28] Yang Z, Xu J, Wang P, Zhuang X, Pan A and Tong L 2011 *Nano Lett.* **11** 5085

[29] Liu R B, Zhuang X J, Xu J Y, Li D B, Zhang Q, Ding K, He P, Ning C, Zou B and Pan A 2011 *Appl. Phys. Lett.* **99** 263101

[30] Zhuang X, Ning C Z and Pan A 2012 *Adv. Mater.* **24** 13

[31] Xu J, Ma L, Guo P, Zhuang X, Zhu X, Hu W, Duan X and Pan A 2012 *J. Am. Chem. Soc.* **134** 12394

[32] Xu J, Zhuang X, Guo P, Zhang Q, Huang W, Wan Q, Hu W, Wang X, Zhu X, Fan C, Yang Z, Tong L, Duan X and Pan A 2012 *Nano Lett.* **12** 5003

[33] Xu J, Zhuang X, Guo P, Huang W, Hu W, Zhang Q, Wan Q, Zhu X, Yang Z, Tong L, Duan X and Pan A 2012 *Sci. Rep.* **2** 820

[34] Wang Y, Xu J, Ren P, Zhang Q, Zhuang X, Zhu X, Wan Q, Zhou H, Hu W and Pan A 2013 *Phys. Chem. Chem. Phys.* **15** 2912

[35] Guo P, Zhuang X, Xu J, Zhang Q, Hu W, Zhu X, Wang X, Wan Q, He P, Zhou H and Pan A 2013 *Nano Lett.* **13** 1251

[36] Guo P, Hu W, Zhang Q, Zhuang X, Zhu X, Zhou H, Shan Z, Xu J and Pan A 2014 *Advanced Materials* **26** 2844

[37] Ma L, Hu W, Zhang Q, Ren P, Zhuang X, Zhou H, Xu J, Li H, Shan Z, Wang X, Liao L, Xu H Q and Pan A 2014 *Nano Lett.* **14** 694

[38] Ren P, Hu W, Zhang Q, Zhu X, Zhuang X, Ma L, Fan X, Zhou H, Liao L, Duan X and Pan A 2014 *Adv. Mater.* **26** 7444

[39] Guo P, Xu J, Gong K, Shen X, Lu Y, Qiu Y, Xu J, Zou Z, Wang C, Yan H, Luo Y, Pan A, Zhang H, Ho J C and Yu K M 2016 *ACS Nano* **10** 8474

[40] Komsa H P and Krasheninnikov A V 2012 *J. Phys. Chem. Lett.* **3** 3652

[41] Rajbanshi B, Sarkar S and Sarkar P 2015 *Physical Chemistry Chemical Physics* **17** 26166

[42] Ersan F, Gökoğlu G and Aktürk E 2015 *J. Phys. Chem. C* **119** 28648

[43] Kou L, Frauenheim T and Chen C 2013 *J. Phys. Chem. Lett.* **4** 1730

[44] Tan C, Zhao W, Chaturvedi A, *et al*. 2016 *Small* **12** 1866

[45] Feng Q, Zhu Y, Hong J, Zhang M, Duan W, Mao N, Wu J, Xu H, Dong F, Lin F, Jin C, Wang C, Zhang J and Xie L 2014 *Adv. Mater.* **26** 2648

[46] Li H, Duan X, Wu X, Zhuang X, Zhou H, Zhang Q, Zhu X, Hu W, Ren P, Guo P, Ma L, Fan X, Wang X, Xu J and Pan A 2014 *J. Am. Chem. Soc.* **136** 3756

[47] Gong Y, Liu Z, Lupini A R, Shi G, Lin J, Najmaei S, Lin Z, Elías A, Berkdemir A, You G, Terrones H, Terrones M, Vajtai R, Pantelides S T, Pennycook S J, Lou J, Zhou W and Ajayan P M 2013 *Nano Lett.* **14** 442

[48] Ma Q, Isarraraz M, Wang C S, *et al*. 2014 *ACS Nano* **8** 4672

[49] Gong Q, Cheng L, Liu C, Zhang M, Feng Q, Ye H, Zeng M, Xie L, Liu Z and Li Y 2015 *ACS Catalysis* **5** 2213

[50] Meiron O E, Houben L and Bar-Sadan M 2015 *RSC Adv.* **5** 88108

[51] Li H, Zhang Q, Duan X, Wu X, Fan X, Zhu X, Zhuang X, Hu W, Zhou H, Pan A and Duan X 2015 *J. Am. Chem. Soc.* **137** 5284

[52] Chen X, Wang Z, Qiu Y, Zhang J, Liu G, Zheng W, Feng W, Cao W, Hu P and Hu W 2016 *J. Mater. Chem. A* **4** 18060

[53] Zhang W, Li X, Jiang T, Song J, Lin Y, Zhu L and Xu X 2015 *Nanoscale* **7** 13554

[54] Feng Q, Mao N, Wu J, Xu H, Wang C, Zhang J and Xie L 2015 *ACS Nano* **9** 7450

[55] Xia B, An L, Gao D, Shi S, Xi P and Xue D 2015 *Cryst. Eng. Comm.* **17** 6420

[56] Mann J, Ma Q, Odenthal P M, *et al*. 2014 *Adv. Mater.* **26** 1399

[57] Kiran V, Mukherjee D, Jenjeti R N and Sampath S 2014 *Nanoscale* **6** 12856

[58] Kou L, Frauenheim T and Chen C 2013 *J. Phys. Chem. Lett.* **4** 1730

[59] Yang Y, Wang S, Zhang J, Li H, Tang Z and Wang X 2015 *Inorganic Chemistry Frontiers* **2** 931

[60] Klee V, Preciado E, Barroso D, Nguyen A, Lee C, Erickson K, Triplett M, Davis B, Lu I, Bobek S, McKinley J, Martinez J, Mann J, Talin A, Bartels L and Léonard F 2015 *Nano Lett.* **15** 2612

[61] Yang H, Zhang T, Zhu H, Zhang M, Wu W and Du M 2016 *International Journal of Hydrogen Energy* **42** 1912

[62] Fu Q, Yang L, Wang W, Han A, Huang J, Du P, Fan Z, Zhang J and Xiang B 2015 *Adv. Mater.* **27** 4732

[63] Huang J, Wang W, Fu Q, Yang L, Zhang K, Zhang J and Xiang B 2016 *Nanotechnology* **27** 13LT01

[64] Duan X, Wang C, Fan Z, Hao G, Kou L, Halim U, Li H, Wu X, Wang Y, Jiang J, Pan A, Huang Y, Yu R and Duan X 2015 *Nano Lett.* **16** 264

[65] Chen Y, Xi J, Dumcenco D O, Liu Z, Suenaga K, Wang D, Shuai Z, Huang Y and Xie L 2013 *Acs Nano* **7** 4610

[66] Azizi A, Wang Y, Lin Z, Wang K, Terrones M, Crespi V and Alem N 2016 *Microscopy and Microanalysis* **22** 1548

[67] Chen Y, Wen W, Zhu Y, Mao N, Feng Q, Zhang M, Hsu H, Zhang J, Huang Y and Xie L 2016 *Nanotechnology* **27** 445705

[68] Yao J, Zheng Z and Yang G W 2016 *ACS Applied Materials & Interfaces* **42** 20872

[69] Chandrasekar H and Nath D N 2015 *Mater. Res. Express* **2** 095007

[70] Lin Z, Thee M T, Elías A L, Feng S, Zhou C, Fujisawa K, Perea-Lopez N, Carozo V, Terrones H and Terrones M 2014 *APL Mater.* **2** 092514

[71] Kim J S, Moran S T, Nayak A P, Pedahzur S, Ruiz I, Ponce G, Rodriguez D, Henny J, Liu J, Lin J and Akinwandeet D 2016 *2D Mater* **3** 025003

[72] Yoshida S, Kobayashi Y, Sakurada R, Mori S, Miyata Y, Mogi H, Koyama T, Takeuchi O and Shigekawa H 2015 *Sci. Rep.* **5** 14808

[73] Wang L, Sofer Z, Luxa J and Pumera M 2015 *Adv. Mater. Interf.* **2**

[74] He J, He D, Wang Y and Zhao H 2015 *Opt. Express* **23** 33370

[75] Xi J, Zhao T, Wang D and Shuai Z 2013 *J. Phys. Chem. Lett.* **5** 285

[76] Li X, Puretzky A A, Sang X, K C S, Tian M, Ceballos F, Mahjouri-Samani M, Wang K, Unocic R R, Zhao H, Duscher G, Cooper V R, Rouleau C M, Geohegan D B and Xiao K 2016 *Adv. Funct. Mater.*

[77] Li X, Lin M W and Puretzky A A 2016 *J. Mater. Res.* **31** 923

[78] Zhang M, Wu J, Zhu Y, Dumcenco D O, Hong J, Mao N, Deng S, Chen Y, Yang Y, Jin C, Chaki S H, Huang Y S, Zhang J and Xie L 2014 *ACS Nano* **8** 7130

[79] Tongay S, Narang D S, Kang J, Fan W, Ko C, Luce A V, Wang K X, Suh J, Patel K D, Pathak V M, Li J and Wu J 2014 *Appl. Phys. Lett.* **104** 012101

[80] Zhang C, KC S, Nie Y, Liang C, Vandenberghe W G, Longo R C, Zheng Y, Kong F, Hong S, Wallace R M and Cho K 2016 *ACS Nano* **10** 7370

[81] Duerloo K A N and Reed E J 2015 *ACS Nano* **10** 289

[82] Yu P, Lin J, Sun L, Le Q L, Yu X, Gao G, Hsu C H, Wu D, Chang T R, Zeng Q, Liu F, Wang Q J, Jeng H T, Lin H, Trampert A, Shen Z, Suenaga K and Liu Z 2016 *Adv. Mater.* **29** 1603991

[83] Liu S, Yuan X, Wang P, Chen Z G, Tang L, Zhang E, Zhang C, Liu Y, Wang W, Liu C, Chen C, Zou J, Hu W and Xiu F 2015 *ACS Nano* **9** 8592

[84] Jung C S, Shojaei F, Park K, Oh J, Im H, Jang D, Park J and Kang K 2015 *ACS Nano* **9** 9585

[85] Zhong X, Zhou W, Zhou Y, Zhou F, Liu C, Yin Y, Peng Y and Tang D 2016 *RSC Adv.* **6** 60862

[86] Liu F, Zheng S, Chaturvedi A, Zólyomi V, Zhou J, Fu Q, Zhu C, Yu P, Zeng Q, Drummond N D and Fan H J 2016 *Nanoscale* **8** 5826

[87] Tan T L, Ng M F and Eda G 2016 *The Journal of Physical Chemistry C* **120** 2501

[88] Li B, Huang L, Zhong M, Huo N, Li Y, Yang S, Fan C, Yang J, Hu W, Wei Z and Li J 2015 *ACS Nano* **9** 1257

[89] Dong S, Liu X, Li X, Kanzyuba V, Yoo T, Rouvimov S, Vishwanath S, Xing H G, Jena D, Dobrowolska M and Furdyna J K 2016 *APL Mater.* **4** 032601

[90] Zhao X, Dai X, Xia C, Wang T and Peng Y 2015 *Solid State Commun.* **25** 1

[91] Çakır D, Sahin H and Peeters F M 2014 *Physical Chemistry Chemical Physics* **16** 16771

[92] Liu X, Zhao X, Ma X, Wu N, Xin Q and Wang T 2016 *Physica E* **87** 6

[93] Westover R D, Atkins R A, Ditto J J and Johnson D C 2014 *Chem. Mater.* **26** 3443

[94] Li Z, Xiao Y, Gong Y, Wang Z, Kang Y, Zu, Ajayan P M, Nordlander P and Fang Z 2015 *ACS Nano.* **9** 10158

[95] Yu Y, Ji Z, Zu S, Du B, Kang Y, Li Z, Zhou Z, Shi K and Fang Z 2016 *Adv. Funct. Mater.* **26** 6394

[96] Li Z, Ye R, Feng R, Kang Y, Zhu X, Tour J M and Fang Z 2015 *Adv. Mater.* **27** 5235